(Received 16 September 2025, Accepted 20 November 2025, Scheduled 10 December 2025)

Multi-Mode Dual Five-Phase Hybrid Excitation Motor High Efficiency Control Based on Gradient Descent

Yu Nan*, Ye Yuan, Zhenzhen Kong, Xiaozhou Yang, Dong Mu, and Fan Yang

Kaifeng Power Supply Company, State Grid Henan Electric Power Company, Kaifeng 475000, China

ABSTRACT: The multi-mode dual five-phase hybrid excitation (MM-DFHE) motor, owing to its unique dual-stator configuration, is capable of operating in four distinct modes, offering exceptional operational flexibility. However, this flexibility introduces a control challenge, particularly in Mode IV where the auxiliary stator acts as both an exciter and a torque producer. The additional current variables in this mode lead to suboptimal current distribution, compromising efficiency and dynamic response. To address this, this paper proposes a novel low-loss current optimization control strategy. The key contribution is a Gradient Descent (GD) based online optimization algorithm that dynamically distributes the auxiliary excitation current, specifically tailored for the improved Mode IV operation. This approach resolves the trade-off between loss minimization and dynamic performance prevalent in conventional methods. Simulated and experimental results demonstrate that the proposed strategy reduces total copper loss by up to 13% compared to conventional methods.

NOMENCLATURE

$\psi_{d/q0}(\psi_{d/q1})$	Main (auxiliary) drive stator winding dq-axis flux linkage
$L_{d/q0}(L_{d/q1})$	Main (auxiliary) drive stator winding dq-axis self-inductance
$i_{d/q0}(i_{d/q1})$	Main (auxiliary) drive stator winding dq-axis current
$\psi_{pm0}(\psi_{pm1})$	Main (auxiliary) drive stator PM flux linkage
ψ_{f0}	Equivalent air gap flux linkage of main drive stator
$u_{d/q0}(u_{d/q1})$	Main (auxiliary) drive stator winding dq-axis voltage
R_{s0}/R_{s1}	Main (auxiliary) drive stator phase resistance
k	The coefficient of influence to the main drive stator air-gap flux linkage during excitation of the auxiliary drive stator winding
ω_e	Electrical angular speed
p	Pole pairs
λ	The Lagrange multiplier
$T_{e0}\,(T_{e1})$	Main (auxiliary) drive output torque
P_{cu}	Copper loss

1. INTRODUCTION

Permanent magnet synchronous motors (PMSMs) have become widely adopted in electric agricultural vehicles owing to their high power density and efficiency [1, 2]. Meanwhile, agricultural vehicles face harsher operating conditions than conventional electric vehicles. They experience large load variations and frequent start-stop operations. However, conventional PMSMs show limited performance in agricultural applications, even with control algorithm optimizations. Due to the limitations of its inherent single-stator winding structure under complex farming conditions, the system performance becomes suboptimal [3]. Conversely, hybrid excitation permanent magnet synchronous motor (HEPMSM) provides an additional degree of freedom for flux linkage regulation. This capability enables flux adjustment and expands the high-efficiency operating region [4, 5]. However, the excitation winding introduces additional copper losses, impairing motor performance. Therefore, subsequent research proposes a dual-stator motor system [6, 7]. The system achieves optimal performance matching under varying operating conditions through coordinated interaction between its unique inner and outer stators. To combine the advantages of both HEPMSMs and dual-stator systems, a multi-mode dual five-phase hybrid excitation motor (MM-DFHEM) is proposed which has four operating modes [8]. Mode I uses only the main drive stator winding to produce torque. Mode II uses only the auxiliary drive stator winding. Mode III uses both stators together for dual-motor operation. Mode IV uses main drive q-axis current and auxiliary d-axis current to control magnetic flux in hybrid excitation operation. Because the motor has a complex design with multiple modes, it needs different control methods for low-speed constant-torque regions and high-speed constant-power regions [9]. Therefore, engineers must develop special control strategies to make this motor work most efficiently in all conditions.

Currently, efficiency optimization control methods for PMSM can be generally categorized into minimum flux control [10], flux trajectory optimization [11], and minimum copper loss (MCL) control [12, 13]. The principle of minimum flux control is to reduce the stator flux amplitude to minimize losses. Ref. [14] adjusts the flux in combination with voltage limit constraints. However, this approach is only applicable under light load [15]. The flux trajectory optimization method balances copper losses by optimizing the dq-axis flux trajectories (e.g., circular or hexagonal) [16]. However, this method

* Corresponding author: Yu Nan (nanyu12024@163.com).

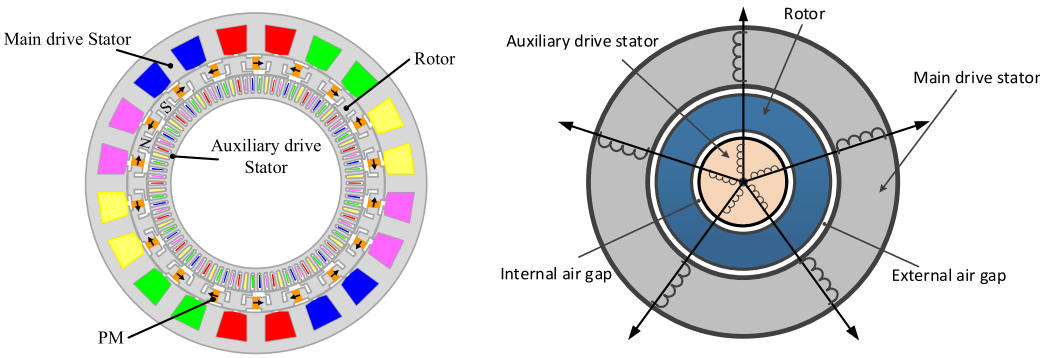

FIGURE 1. MM-DFHE motor topology and simplified model.

uses offline-computed optimal trajectories and online table lookup, limiting dynamic performance [17]. Loss minimization control, characterized by fast response, smooth operation, and strong applicability, is widely used in the optimal control.

However, most of the aforementioned control strategies are typically applied to conventional hybrid excitation machines [18]. The dual-stator motor studied in this paper features a complex structure, where one stator serves as an auxiliary excitation source. Unlike traditional PMSMs, this configuration introduces additional current components, such as dual-port excitation currents and their harmonics [19]. Consequently, the aforementioned methods cannot be directly applied. This limitation arises from the influence of flux linkage between the primary and auxiliary drives, as well as the need for multi-objective optimization. Recently, [20] proposed a copper loss minimization method for dual three-phase permanent magnet machines, such as dual-stator winding configurations. Beyond the dual-stator windings, the MM-DFHE motor also exhibits characteristics of hybrid excitation machines [21]. In [22], a minimum copper loss control algorithm was employed for the constant torque range to derive the relationship between excitation current and torque. It utilizes positive excitation current to enhance the motor's load capacity while minimizing copper losses. However, these strategies exhibit significant limitations when being applied to the MM-DFHE motor. Methods like [10–17] are designed for single-stator or conventional hybrid excitation machines and fail to manage the coordinated current distribution across the dual stators inherent in Modes I–III. More critically, for the most versatile yet complex Mode IV — where the auxiliary stator provides excitation to the main stator while concurrently producing torque — Refs. [20–22] lack a dedicated and effective online optimization framework. The interplay between the main drive q-axis current and auxiliary d-axis excitation current creates a multi-variable optimization problem that offline table-lookup or single-objective approaches cannot dynamically solve, leading to inevitable efficiency loss and sluggish response.

To solve the above issues, this paper proposes a high-efficiency control strategy for a multi-mode dual five-phase hybrid excitation motor (MM-DFHE) optimized via gradient descent. The optimal current is derived using the Lagrange multiplier method to minimize copper losses. Furthermore, this study introduces an improved approach for complex Mode IV, where the auxiliary drive excites the main drive while producing torque. Based on this enhancement, the gradient descent algorithm is employed to further optimize current distribution to achieve higher efficiency and dynamic smoothness. Finally, simulations and experiments validate the effectiveness of the proposed control strategy.

2. STRUCTURE AND MATHEMATICAL MODEL OF MM-DFHE MOTOR

2.1. Motor Topology and Simplified Model

The topology of the MM-DFHE motor is illustrated in Fig. 1. The outer stator is a 5-phase 18-pole 20-slot concentrated winding, referred to as the main drive stator. The inner stator is a 5-phase 18-pole 90-slot distributed winding, termed the auxiliary drive/excitation stator. The rotor adopts a swallowtail structure, with the outer and inner auxiliary salient poles of the intermediate rotor employing unequal and asymmetrically offset designs to suppress torque ripple in both the main and auxiliary drive motors, thereby achieving comprehensive torque ripple suppression across the entire motor.

The simplified motor model reveals that the permanent magnets adopt a radial topology, with radial permanent magnets sandwiched between rotor segments. Adjacent radial permanent magnet modules have opposite magnetization directions, achieving a flux-focusing effect that effectively enhances the motor's torque output capability. Additionally, since the two sets of windings are separately placed in two stators, they exhibit mutual independence. Through flexible control of the dq-axis currents in the outer and inner stator windings, the motor can achieve multiple operating modes.

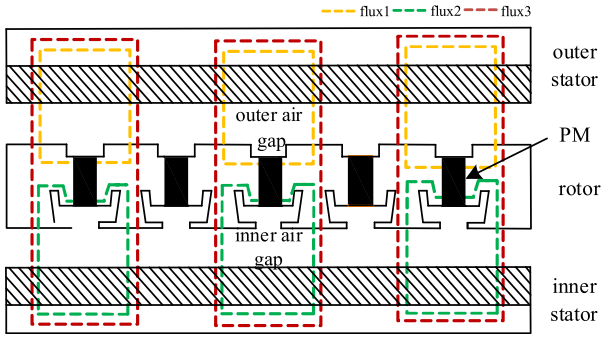

FIGURE 2. MM-DFHE motor flux distribution.

The flux distribution of the MM-DFHE motor is shown in Fig. 2, which contains three main flux paths. The main flux (Flux 1) is produced by the combined action of the main drive winding and permanent magnets, traveling across the outer air-gap and linking with the outer stator winding to form a closed path. The secondary flux (Flux 2) is formed by the interaction between the auxiliary drive winding and permanent magnets, traveling across the inner air-gap and linking with the inner stator winding to form a closed path. The excitation flux (Flux 3) is generated by the joint armature reaction of both main and auxiliary drive windings. This flux is superposed on the permanent magnet flux at the iron core pole, thereby enabling flexible adjustment of the intensity and orientation of the magnetic field in both the inner and outer air-gaps. This multi-path flux distribution design enables flexible flux allocation through independent control of the main and secondary magnetic circuits. The flux paths remain independent while providing a structural basis for motor performance optimization. Precise flux regulation can be achieved by controlling the winding currents.

The MM-DFHE motor operates in four distinct working modes as Table 1 shows. In Mode I, the main drive stator generates torque through q-axis current injection. Mode II employs the auxiliary drive stator to produce torque independently via q-axis current injection. Mode III enables both stators to output torque together using q-axis currents. Mode IV extends Mode III operation by adding d-axis current injection, activating the magnetic field regulation function of the auxiliary drive. This four-mode system achieves flexible control of the dual-stator motor through various current injection combinations.

TABLE 1. Classification of operating modes.

	Mode I	Mode II	Mode III	Mode IV
Armature winding	i_{q0}	0	i_{q0}	i_{q0}
Excitation winding	0	i_{q1}	i_{q1}	i_{d1}

2.2. Mathematical Model

Based on the above analysis, the flux equations of the MM-DFHE motor in the d-q rotating reference frame can be expressed as:

$$\begin{cases} \psi_{d0} = L_{d0} i_{d0} + \psi_{f0} \\ \psi_{q0} = L_{q0} i_{q0} \\ \psi_{d1} = L_{d1} i_{d1} + \psi_{pm1} \\ \psi_{q1} = L_{q1} i_{q1} \end{cases} \tag{1}$$

where $\psi_{d/q0}$ and $\psi_{d/q1}$ represent *dq*-axes flux linkage of the main drive stator winding and auxiliary driven stator winding as subscripts, respectively; $L_{d/q0}$ and $L_{d/q1}$ represent *dq*-axes self-inductance of main drive stator winding and auxiliary drive stator winding, respectively, where $L_{d0} = L_{q0}$ and $L_{d1} = L_{q1}$; $i_{d/q0}$ and $i_{d/q1}$ represent the *dq*-axes currents of the main drive stator winding and auxiliary drive stator winding as subscript, respectively; ψ_{pm1} is the auxiliary drive stator permanent magnet flux linkage; ψ_{f0} is the equivalent air-gap flux linkage of main drive stator, which consists of permanent magnet flux linkage of main drive stator winding and regulating magnetic flux linkage of auxiliary drive excitation winding. ψ_{f0} can be expressed as

$$\psi_{f0} = \psi_{pm0} + k i_{d1} \tag{2}$$

where ψ_{pm0} is the permanent magnet flux linkage of the main drive stator, and k is the coefficient of influence to the main drive stator air-gap flux linkage during excitation of the auxiliary drive stator winding.

The voltage equation for DF-HEPMSM can be expressed as

$$\begin{cases} u_{d0} = (R_{s0} + sL_{d0}) i_{d0} - \omega_e L_{q0} i_{q0} + sk i_{d1} + s\psi_{pm0} \\ u_{q0} = \omega_e L_{d0} i_{d0} + (R_{s0} + sL_{q0}) i_{q0} + \omega_e k i_{d1} + \omega_e \psi_{pm0} \\ u_{d1} = (R_{s1} + sL_{d1}) i_{d1} - \omega_e L_{q1} i_{q1} + s\psi_{pm1} \\ u_{q1} = \omega_e L_{d1} i_{d1} + (R_{s1} + sL_{q1}) i_{q1} + \omega_e \psi_{pm1} \end{cases} \tag{3}$$

where $u_{d/q0}$ and $u_{d/q1}$ represent *dq*-axes voltages of the main drive stator winding and auxiliary drive stator winding as subscripts, respectively; R_{s0} and R_{s1} are phase resistances of the main drive stator and auxiliary drive stator, respectively; ω_e is the electrical angular speed of the motor; s is a differential operator.

The torque of the dual-stator motor system is provided by the two stators. Since the torque equation for one stator matches the equation for a conventional five-phase motor, the resultant torque is

$$\begin{aligned} T_e &= \frac{5}{2} p (i_{q0} \psi_{d0} - i_{d0} \psi_{q0}) + \frac{5}{2} p (i_{q1} \psi_{d1} - i_{d1} \psi_{q1}) \\ &= \frac{5}{2} p (i_{q0} \psi_{d0} - i_{d0} \psi_{q0} + i_{q1} \psi_{d1} - i_{d1} \psi_{q1}) \end{aligned} \tag{4}$$

Since the *dq*-axes inductances of the two sets of windings in this motor are equal and constant, the torque equation can be expressed as:

$$T_e = \frac{5}{2} p \left[(\psi_{pm0} + k i_{d1}) i_{q0} + \psi_{pm1} i_{q1} \right] \tag{5}$$

where p is the number of pole pairs of the motor. The above equation indicates that the total electromagnetic torque is generated by the main drive stator winding and auxiliary drive stator winding, respectively and an extra term in the auxiliary drive stator winding excitation state.

3. MULTI-MODE CONTROL ANALYSIS OF MM-DFHE MOTOR

The MM-DFHE motor operates in four distinct modes. Modes I and II use only one set of armature windings for torque generation, functioning similarly to conventional five-phase permanent magnet motors. In contrast, Modes III and IV employ both winding sets for simultaneous torque output, where current and torque distributions directly affect copper losses. To address this, the study develops an optimal torque distribution strategy using Lagrange multipliers to achieve minimum copper loss control. Furthermore, the efficiency characteristics of all four operating modes are analyzed, establishing the motor's high-efficiency operational range.

3.1. Minimum Copper Loss Control

The Lagrange multiplier method solves optimization problems with constraints. This method forms the core of the minimum copper loss control algorithm. It introduces a multiplier λ to combine the objective function and constraints into new equations. The final solution set optimizes the objective function under given constraints.

This study uses the torque equation (5) as the constraint and copper loss equation (6) as the objective function. Based on these constraints and objective function, the Lagrange equation (7) for minimum copper loss optimization is derived

$$P_{cu} = \frac{5}{2}R_{s0}(i_{d0}^2 + i_{q0}^2) + \frac{5}{2}R_{s1}(i_{d1}^2 + i_{q1}^2) \tag{6}$$

$$L(i_{d0}, i_{q0}, i_{d1}, i_{q1}) = \frac{5}{2}R_{s0}(i_{d0}^2 + i_{q0}^2) + \frac{5}{2}R_{s1}(i_{d1}^2 + i_{q1}^2)$$
$$+\lambda\left\{T_e - \frac{5}{2}p\left[(\psi_{pm0} + ki_{d1})i_{q0} + \psi_{pm1}i_{q1}\right]\right\} \tag{7}$$

In Equation (7), λ represents the Lagrange multiplier. Partial derivatives of Equation (7) are taken with respect to i_{d0}, i_{q0}, i_{d1}, i_{q1}, and λ, then set equal to 0 to get the resulting.

3.2. Improved Mode IV Based on Gradient Descent

The previous section analyzes the current distribution for minimum copper loss in each operating mode. Mode III involves simultaneous torque output from both main and auxiliary drives, while Mode IV combines main drive torque production with auxiliary drive excitation. By solving the simultaneous torque equation (5) and copper loss equation (6) through the Lagrange function, the current distribution relationships for these two modes are obtained:

$$i_{q0} = \frac{R_{s1}}{R_{s0}} \cdot \frac{\psi_{pm0}}{\psi_{pm1}} \cdot i_{q1} \tag{8}$$

$$i_{d1} = -\frac{\psi_{pm0}}{2k} - \sqrt{\frac{R_{s0}}{R_{s1}} \cdot i_{q0}^2 + \frac{\psi_{pm0}^2}{4k^2}} \tag{9}$$

Substituting Equation (9) into the torque equation yields:

$$\begin{cases} i_{d0} = 0 \\ i_{q1} = 0 \\ i_{q0} = \frac{4R_{s1}T_e^2}{R_{s0}(5kp)^2 i_{q0}^3 + 10R_{s1}p\psi_{pm0}T_e} \\ i_{d1} = \frac{4kR_{s0}T_e^2}{R_{s1}(5p)^2(\psi_{pm0}+ki_{d1})^3} \end{cases} \tag{10}$$

By flexibly controlling d- and q-axis currents, the motor can be configured into several distinct operational modes, the torque equations for which are summarized in Table 2.

Equation (10) reveals the complex relationship between torque and currents i_{q0} and i_{d1} in Mode IV. These current variables are substituted into the copper loss expression. Data fitting then produces the specific torque relationship displayed in Fig. 3.

TABLE 2. Classification of operating modes.

Mode	Torque Equation
Mode I	$T_e = 2.5p\psi_{pm0}i_{q0}$
Mode II	$T_e = 2.5p\psi_{pm1}i_{q1}$
Mode III	$T_e = 2.5p\left(\psi_{pm0}i_{q0} + \psi_{pm1}i_{q1}\right)$
Mode IV	$T_e = 2.5p\left[(\psi_{pm0} + ki_{d1})i_{q0} + \psi_{pm1}i_{q1}\right]$

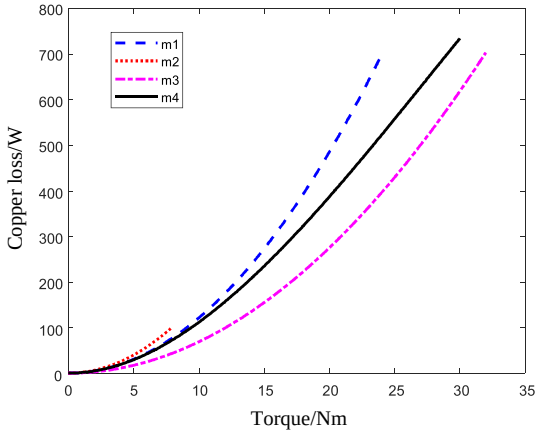

FIGURE 3. Torque-copper loss characteristics under different operating modes.

Figure 3 shows that Mode III achieves the minimum copper loss under rated motor conditions. Considering only copper loss without efficiency, Mode III becomes the sole candidate. To demonstrate operational flexibility in copper loss performance, this study improves Mode IV by optimizing current distribution while maintaining the auxiliary drive's excitation function for the main drive.

The improved Mode IV introduces an additional current component for allocation, requiring distribution of three current components. Using the Lagrange multiplier method for this calculation would significantly increase computational complexity. Moreover, achieving fast motor performance requires offline computation of the resulting currents, which further increases workload. Therefore, this approach combines the gradient descent method with torque equivalence between time steps k and $k+1$. The current gradient operator ∇ relates to the currents at time step $k+1$ as follows:

$$\begin{cases} \nabla(i) = (5R_{s0}i_{q0}, 5R_{s1}i_{d1}, 5R_{s1}i_{q1}) \\ i^{k+1} = i^k + \alpha\nabla(i^k) \end{cases} \tag{11}$$

Here, α represents the gradient descent step size. This yields the current expressions at time step $k+1$:

$$\begin{cases} i_{q0}^{k+1} = i_{q0}^k - 5\alpha R_{s0}i_{q0}^k \\ i_{d1}^{k+1} = i_{d1}^k - 5\alpha R_{s1}i_{d1}^k \\ i_{q0}^{k+1} = i_{q1}^k - 5\alpha R_{s1}i_{q1}^k \end{cases} \tag{12}$$

The torque expressions for Mode IV at time steps k and $k+1$ are:

$$\begin{aligned} T_{e4}^{*k} &= \frac{5}{2}p\left[(\psi_{pm0}+ki_{d1}^{k})i_{q0}^{k}+\psi_{pm1}i_{q1}^{k}\right] \\ T_{e4}^{*k+1} &= \frac{5}{2}p\left[(\psi_{pm0}+ki_{d1}^{k+1})i_{q0}^{k+1}+\psi_{pm1}i_{q1}^{k+1}\right] \end{aligned} \tag{13}$$

The iterative formula in Equation (11) demonstrates:

$$\begin{aligned} T_{e4}^{*k} &= T_{e4}^{*k+1} = T_{e4}^{*k}+\frac{5}{2}p\Big\{-5\alpha R_{s0}[\psi_{pm0}+ki_{d1}^{k}]i_{q0}^{k} \\ &\quad -5\alpha kR_{s1}i_{d1}^{k}i_{q0}^{k}+5^{2}\alpha^{2}kR_{s0}R_{s1}i_{d1}^{k}i_{q0}^{k} \\ &\quad -5\alpha\psi_{pm1}R_{s1}i_{q1}^{k}\Big\} \end{aligned} \tag{14}$$

When the iteration period is sufficiently small, the torque at time k approximately equals the torque at time $k+1$. Setting the latter part of Equation (14) to yields i_{d1} at time k

$$i_{d1}^{k} = \frac{\psi_{pm0}R_{s0}i_{q0}^{k}+\psi_{pm1}R_{s1}i_{q1}^{k}}{[k(5\alpha R_{s0}R_{s1}-R_{s0}-R_{s1})]\,i_{q0}^{k}} \tag{15}$$

The torque provided by the auxiliary drive excitation is obtained by substituting the expression for i_{d1} into the torque equation (13):

$$\begin{aligned} T_{e4}^{*k} &= \frac{5}{2}p\left[\psi_{pm0}i_{q0}^{k}+\psi_{pm1}i_{q1}^{k}+\frac{\psi_{pm0}R_{s0}i_{q0}^{k}+\psi_{pm1}R_{s1}i_{q1}^{k}}{5\alpha R_{s0}R_{s1}-R_{s0}-R_{s1}}\right] \\ &= T_{e3}^{k}+\frac{5}{2}p\frac{\psi_{pm0}R_{s0}i_{q0}^{k}+\psi_{pm1}R_{s1}i_{q1}^{k}}{5\alpha R_{s0}R_{s1}-R_{s0}-R_{s1}} \end{aligned} \tag{16}$$

To ensure the stability and convergence of the online gradient descent algorithm, careful consideration is given to the selection of the step size α and stopping criterion. The step size is chosen based on the Lipschitz constant L of the gradient of the cost function (copper loss) to satisfy the condition $0 < \alpha < 2/L$, which guarantees a decrease in the objective function at each iteration. For the MM-DFHE motor model studied here, the value $\alpha = 0.05$ was found to satisfy this condition across the expected operating range and was used in both simulations and experiments.

The convergence of the algorithm for each control update is determined by checking the norm of the current vector change, $\Delta i = i_{k+1} - i_k$. The iteration stops when $\|\Delta i\| < \varepsilon$, where ε is a small positive tolerance ($\varepsilon = 0.001$ A is used in this work). This ensures that the solution is sufficiently close to the local optimum within one control cycle. The stability of the optimization process is inherently guaranteed by the convexity of the copper loss function with respect to the currents i_{q0} and i_{d1} in the feasible operating region, ensuring that the gradient descent converges to the global minimum loss point.

4. SIMULATION VERIFICATION

In the simulation, the initial excitation current i_{d1} for Mode IV was set to -5 A. This value was determined as an empirical starting point through preliminary Lagrangian optimization and simulation sweeps, conducted under the constraints of ensuring magnetic circuit non-saturation, adhering to current limits, and meeting the output torque requirements. In the improved Mode IV control strategy, this value serves as the initial starting point for the gradient descent algorithm, which is used to perform online dynamic optimization of the current distribution, thereby achieving lower copper loss and faster dynamic response.

To verify the feasibility of the control theory in Section 3, this study develops a MATLAB/Simulink simulation model for current (torque) distribution control under minimum copper loss constraints. The motor parameters used in the simulation are listed in Table 3.

TABLE 3. Parameters of the MM-DFHE.

Main drive parameters	Values	Auxiliary drive parameters	Values
P_{N0}/kW	1.5	P_{N1}/kW	1.0
I_{N0}/A	10	I_{N1}/A	10
R_{s0}/Ω	1.47	R_{s1}/Ω	0.69
Ψ_{pm0}/W_b	0.088	Ψ_{pm1}/W_b	0.031
$L_{d0}(L_{q0})$/H	0.0345	$L_{d1}(L_{q1})$/H	0.003
Number of pair poles/p	9	Excitation coefficient/k	-0.003
Rated speed/rpm	600	Rated Torque/Nm	30.5

The control system block diagram appears in Fig. 4. The variable M selects the operating mode among the four available options. Table 4 gives the relationship between the current distribution for each mode and the total current output from the speed loop PI regulator. The design requires two separate drive circuits because the motor has dual stator windings with isolated neutral points current distribution of improved modes.

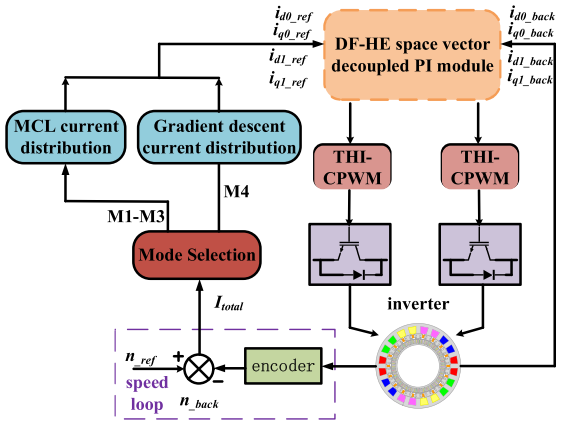

FIGURE 4. Control system block diagram.

The simulation first verifies the mathematical model of the motor. The analysis then calculates the current distribution for minimum copper loss in each operating mode. A comparison follows between the optimal currents from the minimum copper loss algorithm and traditional Maximum Torque Per Ampere (MTPA) strategy under Mode I conditions, confirming the

TABLE 4. Current distribution of improved modes.

	Model I	Model II	Model III	Model IV
Main	$i_{d0} = 0$	$i_{d0} = 0$	$i_{d0} = 0$	$i_{d0} = 0$
drive	$i_{q0} = I_{total}$	$i_{d0} = 0$	$i_{q0} = I_{total} - i_{q1}$	$i_{q0} = I_{total} - i_{q1}$
auxiliary	$i_{d1} = 0$	$i_{d1} = 0$	$i_{d1} = 0$	$i_{d1} = -5\,\mathrm{A}$
drive	$i_{d1} = 0$	$i_{q1} = I_{total}$	$i_{q1} = I_{total} - i_{q0}$	$i_{q1} = I_{total} - i_{q0}$

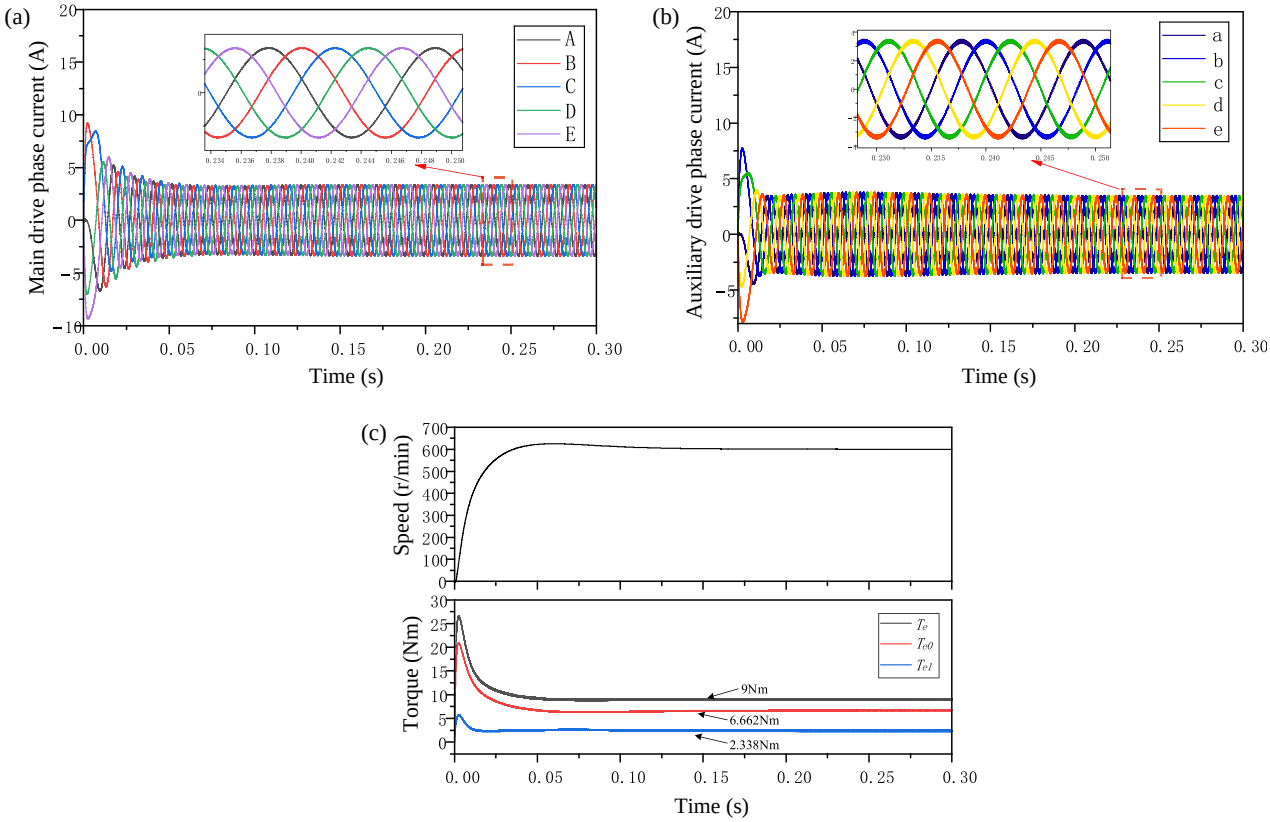

FIGURE 5. Validation of the MM-DFHE motor mathematical model. (a) Main drive phase current. (b) Auxiliary drive phase current. (c) Speed and torque.

algorithm effectiveness. The verification concludes with dynamic performance tests of the improved Mode IV using the gradient descent algorithm.

Figure 5 shows the phase current waveforms of both main and auxiliary drives, along with speed and torque output waveforms. The motor operates under given conditions of 600 rpm speed and 9 Nm load. The labels T_e, T_{e0}, and T_{e1} represent total output torque, main stator winding torque, and auxiliary stator winding torque respectively. The waveforms demonstrate coordinated operation characteristics of the dual-winding system. Simulation data indicate that the total output torque T_e maintains precise 9 Nm load demand. The main drive contributes $T_{e0} = 6.662\,\mathrm{Nm}$ while the auxiliary drive provides $T_{e1} = 2.338\,\mathrm{Nm}$, achieving a 2.85 : 1 torque distribution ratio. For current components, both windings share equal q-axis currents ($i_{q0} = i_{q1} = 3.364\,\mathrm{A}$) with zero d-axis currents ($i_{d0} = i_{d1} = 0$), consistent with Mode III parameter settings. The stable phase current output and corresponding torque tracking validate the correctness of the mathematical model implementation.

Figure 6 presents the simulation results of dq-axis currents for Modes I to IV. The labels i_{d0}, i_{q0}, i_{d1}, and i_{q1} denote the dq-axis currents of the main and auxiliary stator windings. The simulation tests the motor under 400 rpm speed and 6 Nm load. In Fig. 6(a), i_{q0} measures 3.03 A while i_{d0}, i_{d1}, and i_{q1} remain 0 A, matching Mode I requirements. Fig. 6(b) shows i_{q1} at 8.6 A with i_{d0}, i_{d1}, and i_{q0} at 0 A. Fig. 6(c) demonstrates i_{q0} and i_{q1} both at 2.75 A, $i_{d0} = i_{d1} = 0\,\mathrm{A}$, confirming combined output from both windings. Fig. 6(d) reveals i_{q0} and i_{q1} at 2 A, i_{d0} at 0 A, and i_{d1} at -5 A, where the excitation current i_{d1} modifies the main air-gap magnetic field. Compared to Fig. 6(c), the q-axis currents decrease by 0.75 A, highlighting differences from Mode III.

Figure 7 compares the copper losses between the minimum copper loss control algorithm and the traditional MTPA algorithm in Mode I at 400 rpm with 15 Nm load. The auxiliary drive does not participate in output, so $P_{cu1} = 0$. Under this

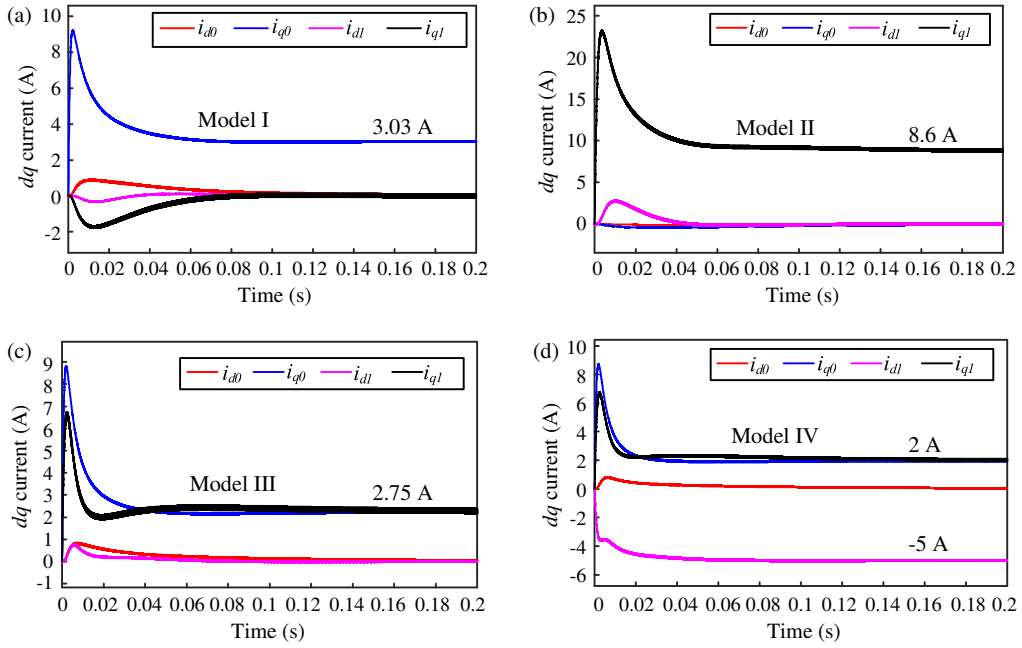

FIGURE 6. Distribution of dq-axis current in each mode.

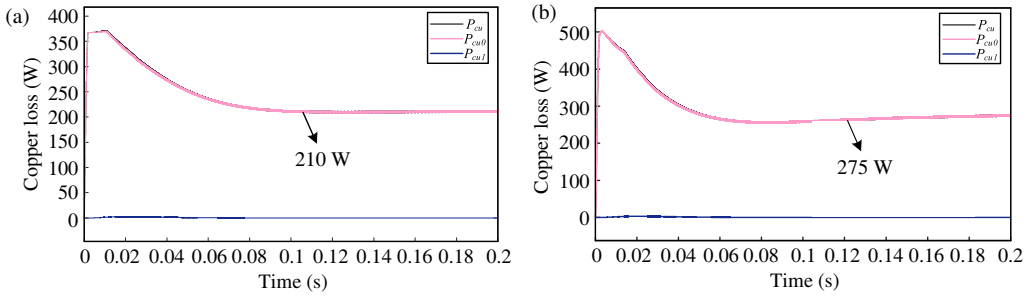

FIGURE 7. Copper consumption simulation comparison. (a) Minimum copper loss control. (b) Traditional MTPA algorithm.

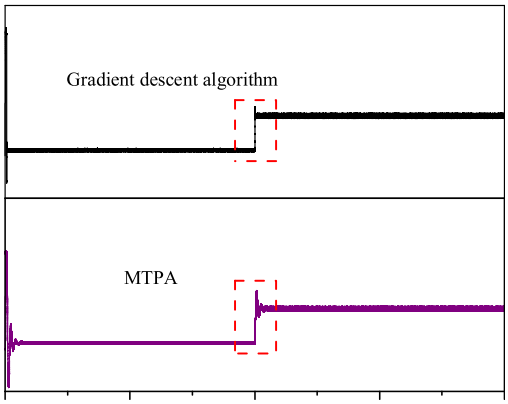

FIGURE 8. Local magnification of d-axis current.

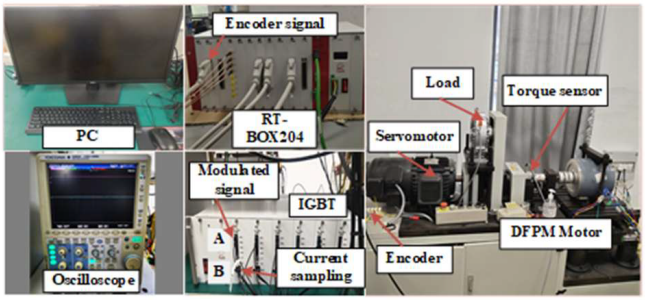

FIGURE 9. Control system experimental platform.

condition, the proposed minimum copper loss control reduces the total copper loss to 210 W, achieving a significant reduction of 23.6% compared to the 275 W produced by the traditional MTPA method. This result verifies the effectiveness of the MCL control strategy.

Figure 8 compares the d-axis current waveforms between the gradient descent method and traditional MTPA algorithm in a magnified view. The comparison reveals significantly reduced current ripple in the gradient descent approach while maintaining identical current trends. This improvement enables optimal solutions for both local and global conditions, ensuring faster motor response and better dynamic performance. These results confirm the effectiveness of the proposed method.

5. EXPERIMENTAL VERIFICATION

To further verify the theoretical and simulation results, Fig. 9 shows the experimental platform. The key hardware components and their specifications are summarized in Table 5. The magnetic powder brake provides motor load. The current sensors operate at 10 kHz sampling frequency and the inverter switches at 10 kHz. The torque sensor model T8-20-B4A/20 Nm measures motor output. The RT-BOX 204 drive system features modular design, where each module contains inverter circuits and sampling circuits. These modules convert Pulse Width Modulation (PWM) signals to AC signals to drive the motor.

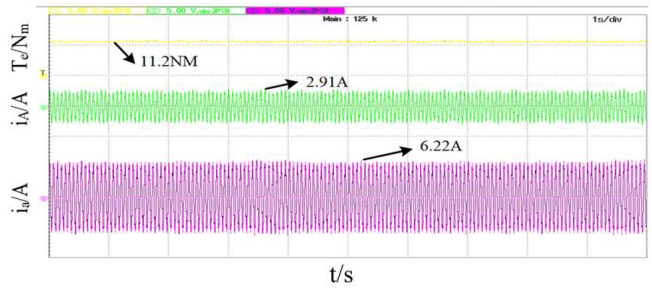

FIGURE 10. MM-DFHE motor current experiment waveforms.

TABLE 5. Experimental platform key parameters.

Category	Value/Specification
Digital Controller	RTU-Box205
PWM Sampling Frequency	10 kHz
Motor Type	MM-DFPM
Torque Sensor	T8-20-B4A(20 Nm)
Inverter	RTM-PEH8035IF (10)
Encoder	Photoelectric Encoder

Figure 10 displays the experimental waveforms of the MM-DFHE motor. The results show non-zero values for both the main drive q-axis current i_{q0} and auxiliary drive q-axis current i_{q1}. These measurements confirm simultaneous torque production from both drives. The current distribution follows the minimum copper loss principle, which verifies the correctness of the current allocation algorithm.

Figure 11 demonstrates the dynamic performance during torque transients in the improved Mode IV, representing the most complex scenario. The experiment operates the motor at 100 rpm while increasing the load from 4.17 Nm to 7.42 Nm. The phase current of the main drive stator winding exhibits a much faster response, stabilizing in 0.6 s compared to the 2.2 s required for the auxiliary drive winding. The results show both stator windings maintain highly sinusoidal phase current waveforms after torque stabilization, indicating excellent dynamic stability. Fig. 12 reveals that the motor output torque closely tracks the load command with a response time of merely 0.5 seconds, validating its superior dynamic performance.

Figure 13 shows the nonlinear experimental fitting curve for MCL control. The motor torque output exhibits multi-value characteristics, making the analytical solution represent a functional relationship of electromagnetic torque T_e. To optimize real-time computation efficiency, the method combines

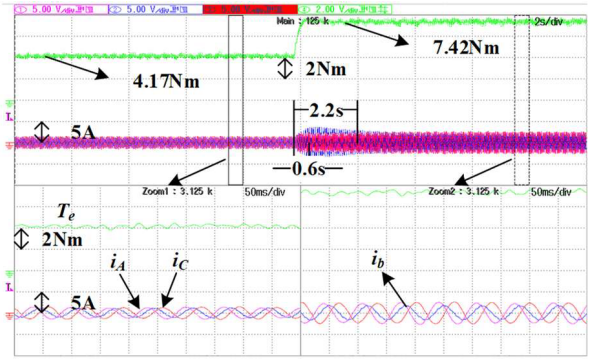

FIGURE 11. Steady-state current before and after torque transients.

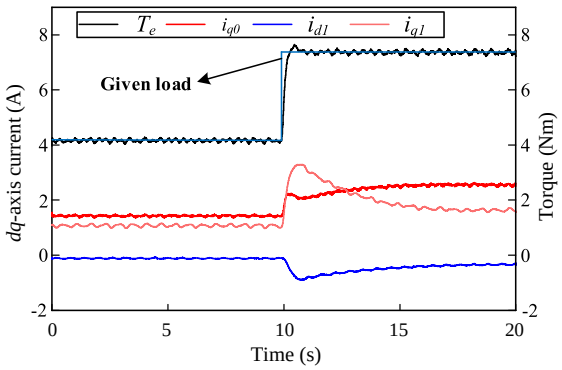

FIGURE 12. dq-axis currents during torque transients.

offline calculation with curve fitting. Numerical analysis tools first solve optimal solutions under different torque conditions. High-order polynomials then perform parametric fitting. The control algorithm directly embeds the fitted analytical expressions, reducing computational load and saving memory resources. The fitting equations for all four current variables in the figure achieve determination coefficients (R^2) exceeding 0.99. These results confirm that the nonlinear regression model delivers excellent fitting accuracy and engineering applicability, with successful fitting outcomes.

Figure 14 compares motor performance under Mode III operation at 100 rpm with step-load increasing from 1 Nm to 20 Nm. Fig. 14(a) and Fig. 14(b) display differences between conventional maximum torque per ampere (MTPA) and the proposed minimum copper loss algorithm in main stator current and copper loss. Experimental measurements show that the minimum copper loss algorithm achieves 205.91 W total loss, significantly lower than the 260.95 W from conventional MTPA. The copper loss difference between methods follows quadratic growth with increasing load, demonstrating the superiority of the proposed current distribution strategy. These results prove the new algorithm delivers better energy efficiency than MTPA across the tested load range.

Figure 15 compares the copper losses between the improved Mode IV with gradient descent optimization and the original Mode IV under different loads. The results show that the improved Mode IV consistently achieves lower copper losses than the original version when using the same step size α. This performance difference validates the correctness of the proposed algorithm.

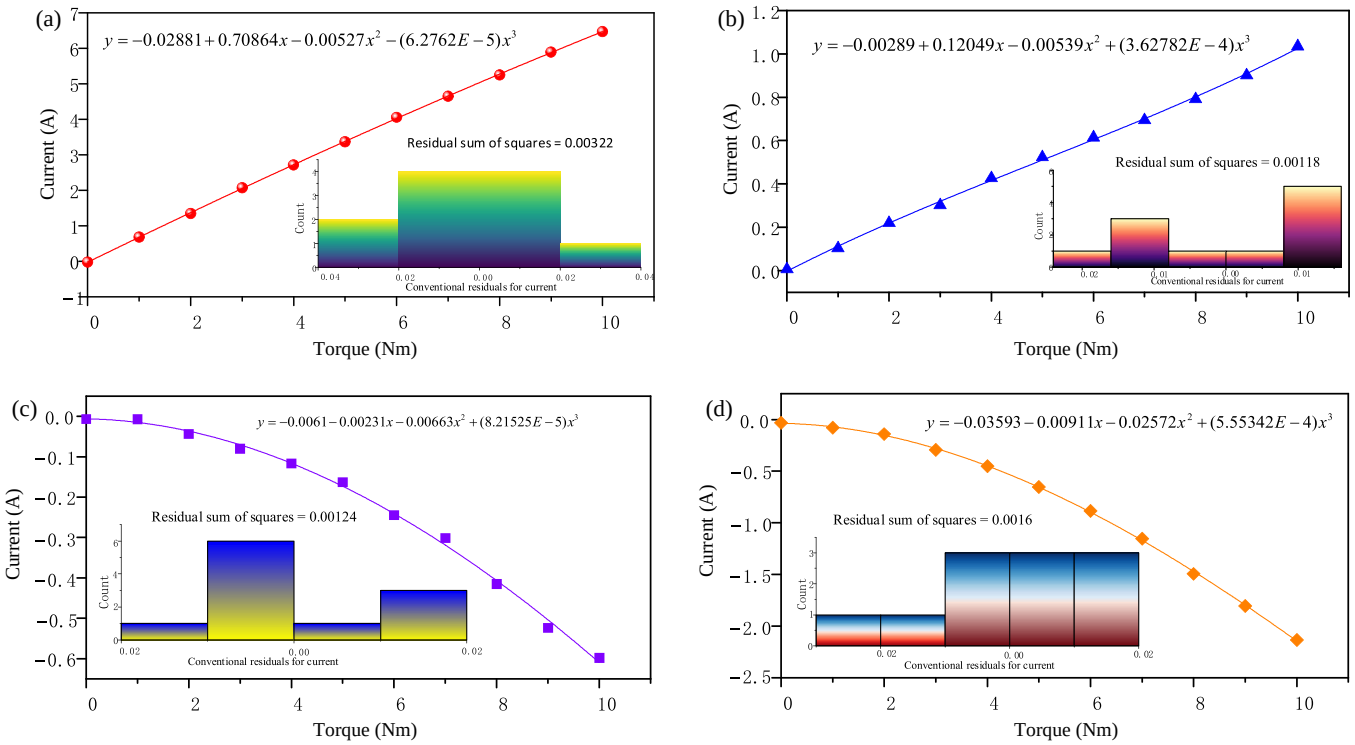

FIGURE 13. Experimental fitting curves of individual components. (a) i_{q0} curve fitting. (b) i_{q1} curve fitting. (c) i_{d0} curve fitting. (d) i_{d1} curve fitting.

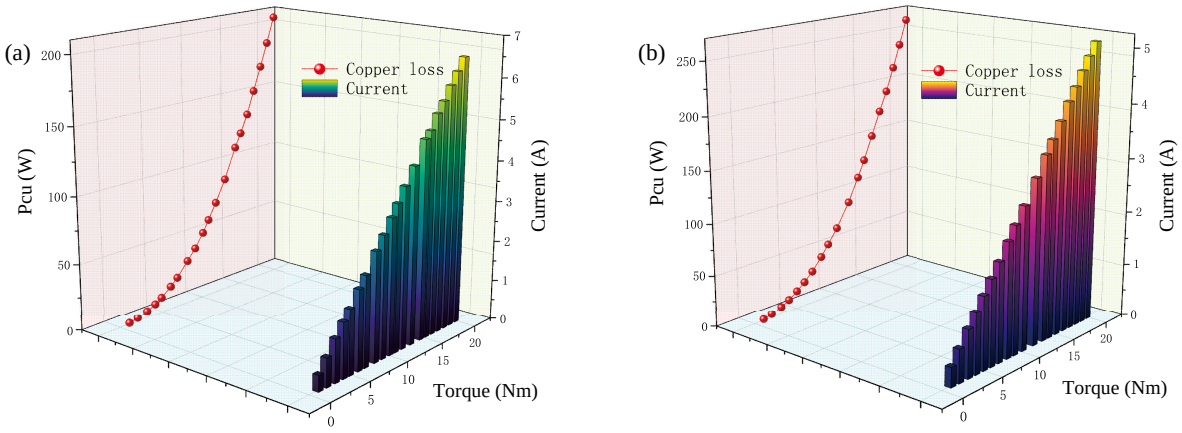

FIGURE 14. Copper consumption comparison chart. (a) MCL. (b) MTPA.

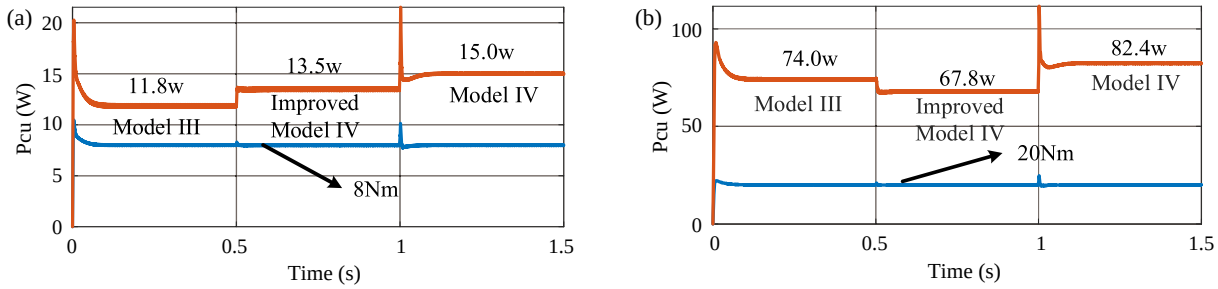

FIGURE 15. Comparative analysis of copper losses across modes under torque transients. (a) Copper loss comparison at 8 Nm. (b) Copper loss comparison at 20 Nm.

6. CONCLUSIONS

In this article, an MM-DFHE motor was proposed to meet agricultural vehicles with complex operational requirements. To fully utilize the performances of this new type of motor, an optimal control strategy was proposed. First, the method establishes a mathematical model of the DF-HEPMSM. Second, the motor operation is divided into four modes to address diverse working conditions. Thereafter, the Lagrange multiplier method calculates optimal currents to minimize copper losses. For complex Mode IV, the approach implements gradient descent optimization. Compared to the original Mode IV strategy, the proposed method reduces copper losses by up to 17%; Finally, experimental confirmed its effectiveness: 1) The solution maintains fast dynamic response despite increased current variables. 2) The motor achieves higher efficiency with lower losses.

ACKNOWLEDGEMENT

This work was supported by State Grid Henan Electric Power Company Science and Technology Project (521790250002).

REFERENCES

[1] Guo, L., W. Xu, N. Jin, and H. Xiao, "A DC-offset removed sensorless control method for PMSM based on SMO with an improved pre-filter and a speed immune position error compensation strategy," *IEEE Transactions on Power Electronics*, Vol. 40, No. 4, 5163–5176, 2025.

[2] Zhang, H., P. Ran, and Z. Zhang, "PMSM sensorless control based on super-twisting algorithm sliding mode observer with the IAORLS parameter estimations," *Scientific Reports*, Vol. 15, No. 1, 22386, 2025.

[3] Liu, H., S. Yan, Y. Shen, C. Li, Y. Zhang, and F. Hussain, "Model predictive control system based on direct yaw moment control for 4WID self-steering agriculture vehicle," *International Journal of Agricultural and Biological Engineering*, Vol. 14, No. 2, 175–181, 2021.

[4] Sun, J., Z. Wang, S. Ding, J. Xia, and G. Xing, "Adaptive disturbance observer-based fixed time nonsingular terminal sliding mode control for path-tracking of unmanned agricultural tractors," *Biosystems Engineering*, Vol. 246, 96–109, 2024.

[5] Wang, X., Z. Wan, L. Tang, W. Xu, and M. Zhao, "Electromagnetic performance analysis of an axial flux hybrid excitation motor for HEV drives," *IEEE Transactions on Applied Superconductivity*, Vol. 31, No. 8, 1–5, Nov. 2021.

[6] Liang, G., S. Huang, W. Liao, Z. Zhang, Y. Liu, C. Feng, X. Wu, and S. Huang, "An optimized modulation of torque and current harmonics suppression for dual three-phase PMSM," *IEEE Transactions on Transportation Electrification*, Vol. 10, No. 2, 3443–3454, Jun. 2024.

[7] Zou, J., C. Liu, Y. Xu, and G. Yu, "A high-precision model for dual three-phase PMSM considering the effect of harmonics, magnetic saturation, and electromagnetic coupling," *IEEE Transactions on Transportation Electrification*, Vol. 10, No. 2, 2456–2468, Jun. 2024.

[8] Chen, Q., H. Wang, Z. Sang, W. Qian, G. Liu, G. Xu, and Z. Liu, "A multi-mode high-efficiency fault-tolerant permanent magnet machine," *IEEE Transactions on Energy Conversion*, Vol. 38, No. 3, 1999–2010, Sep. 2023.

[9] Yan, W., D. Zhang, H. Li, *et al.*, "A hybrid control system for multi-mode double stator switched reluctance motor," in *Proceedings of the CSEE*, Vol. 44, No. 19, 7829–7840, Xi'an, China, 2024.

[10] Hu, X., Y. Li, C. Lv, and Y. Liu, "Optimal energy management and sizing of a dual motor-driven electric powertrain," *IEEE Transactions on Power Electronics*, Vol. 34, No. 8, 7489–7501, Aug. 2018.

[11] Petkar, S. G. and V. K. Thippiripati, "A novel duty-controlled DTC of a surface PMSM drive with reduced torque and flux ripples," *IEEE Transactions on Industrial Electronics*, Vol. 70, No. 4, 3373–3383, Apr. 2023.

[12] Liu, Y., M. Lyu, S. Huang, W. Liao, G. Liang, C. Feng, X. Wu, and S. Huang, "Direct torque control schemes for dual three-phase PMSM considering unbalanced DC-link voltages," *IEEE Transactions on Energy Conversion*, Vol. 39, No. 1, 229–242, Mar. 2024.

[13] Chen, Z., S. Jin, Y. Shen, and M. Wang, "Loss minimum control of surface permanent magnet synchronous motor based on virtual complementary square wave signal injection," *IEEE Journal of Emerging and Selected Topics in Power Electronics*, Vol. 13, No. 4, 5286–5295, Aug. 2025.

[14] De Kock, H. W., A. J. Rix, and M. J. Kamper, "Optimal torque control of synchronous machines based on finite-element analysis," *IEEE Transactions on Industrial Electronics*, Vol. 57, No. 1, 413–419, Jan. 2010.

[15] Bolognani, S., L. Peretti, M. Zigliotto, and E. Bertotto, "Commissioning of electromechanical conversion models for high dynamic PMSM drives," *IEEE Transactions on Industrial Electronics*, Vol. 57, No. 3, 986–993, Mar. 2010.

[16] Alzayed, M. and H. Chaoui, "Efficient simplified current sensorless dynamic direct voltage MTPA of interior PMSM for electric vehicles operation," *IEEE Transactions on Vehicular Technology*, Vol. 71, No. 12, 12 701–12 710, Dec. 2022.

[17] Liu, G., Z. Chen, L. Xu, T. Jiang, and L. Chang, "MTPA control for DC-biased hybrid excitation machine using MTPA control law and virtual signal injection," *IEEE Transactions on Transportation Electrification*, Vol. 10, No. 1, 1571–1582, Mar. 2024.

[18] Dianov, A., F. Tinazzi, S. Calligaro, and S. Bolognani, "Review and classification of MTPA control algorithms for synchronous motors," *IEEE Transactions on Power Electronics*, Vol. 37, No. 4, 3990–4007, Apr. 2022.

[19] Hang, J., H. Wu, S. Ding, Y. Huang, and W. Hua, "Improved loss minimization control for IPMSM using equivalent conversion method," *IEEE Transactions on Power Electronics*, Vol. 36, No. 2, 1931–1940, Feb. 2021.

[20] Wang, X., Z. Wang, M. He, Q. Zhou, X. Liu, and X. Meng, "Fault-tolerant control of dual three-phase PMSM drives with minimized copper loss," *IEEE Transactions on Power Electronics*, Vol. 36, No. 11, 12 938–12 953, Nov. 2021.

[21] Xu, Y., B. Zheng, G. Wang, H. Yan, and J. Zou, "Current harmonic suppression in dual three-phase permanent magnet synchronous machine with extended state observer," *IEEE Transactions on Power Electronics*, Vol. 35, No. 11, 12 166–12 180, Nov. 2020.

[22] Xu, L., H. Ren, T. Jiang, G. Liu, and W. Zhao, "Minimum copper loss fault-tolerant control of zero phase shift dual three-phase SPMSM by using reduced-order transformation matrices," *IEEE Transactions on Energy Conversion*, Vol. 39, No. 4, 2621–2630, Dec. 2024.